Pattern phase diagram for two-dimensional arrays of coupled limit-cycle oscillators

Roland Lauter,[1,2] Christian Brendel,[1] Steven J. M. Habraken,[1] and Florian Marquardt[1,2]

[1]*Institut für Theoretische Physik II, Friedrich-Alexander-Universität Erlangen-Nürnberg, Staudtstr. 7, 91058 Erlangen, Germany*
[2]*Max Planck Institute for the Science of Light, Günther-Scharowsky-Straße 1/Bau 24, 91058 Erlangen, Germany*

Arrays of coupled limit-cycle oscillators represent a paradigmatic example for studying synchronization and pattern formation. We find that the full dynamical equations for the phase dynamics of a limit-cycle oscillator array go beyond previously studied Kuramoto-type equations. We analyze the evolution of the phase field in a two-dimensional array and obtain a "phase diagram" for the resulting stationary and nonstationary patterns. Our results are of direct relevance in the context of currently emerging experiments on nano- and optomechanical oscillator arrays, as well as for any array of coupled limit-cycle oscillators that have undergone a Hopf bifurcation. The possible observation in optomechanical arrays is discussed briefly.

I. INTRODUCTION

Synchronization is an important concept in many branches of physics, chemistry, biology, and other sciences [1]. Within the past three years, a number of experiments have demonstrated for the first time synchronization between two nanomechanical oscillators [2,3], two micromechanical oscillators [4], and in small arrays of the latter [5]. These systems are driven through a Hopf bifurcation into a limit-cycle oscillation, where the energy pump is supplied through feedback or an optical drive. Future, large arrays of synchronized mechanical Hopf oscillators promise to provide robustness against both disorder and noise. Considerable theoretical attention has recently been devoted to the problem of synchronization in arrays, both on the general level and for predicting the behavior of specific systems (e.g., in nanomechanics [6–11] or trapped ion systems [12]). Some progress has also been made in the quantum regime [13–17]. It is efficient to focus on the dynamics of the crucial phase degree of freedom, where the most prominent phenomenological model is the one introduced by Kuramoto [18,19], which more recently has been supplemented by so-called reactive terms [7,20].

In the present work, we will explore synchronization and deterministic pattern formation for a two-dimensional array of identical Hopf oscillators. We present the complete effective model for the phase dynamics in Sec. II. Starting from the widely applicable model of coupled limit-cycle oscillators, we find that the classical phase evolution is affected by extra contributions beyond those investigated previously. These can have a significant impact on the dynamics. Our simulations of the effective model reveal various stationary and nonstationary patterns in different parameter regimes. Phase correlators, length scales, and macroscopic pattern dynamics will be discussed in Sec. III. These are relevant for determining whether an array can easily settle into a phase-locked state, which is important for applications.

There is already a sizable literature on the rich nonlinear dynamics of pattern-forming systems, including spiral dynamics (see [21,22] and references therein). The main point of our paper is the presentation and investigation of a model which will be of importance because it is the model that arises generically for coupled limit-cycle (Hopf) oscillators. This comprises a large class of physical systems, including those studied in the context of the synchronization dynamics of opto- and nanomechanical oscillators.

In the future, one could couple many of those optomechanical oscillators to build large optomechanical arrays [8,14,23–25]. The properties of these devices have been investigated theoretically recently, both for global coupling [9,26–29] and local coupling [30–34]. Pattern formation in the mechanical phases can only be observed for locally coupled oscillators, which would show up naturally in optomechanical crystals [35–37]. In Sec. IV, we will describe optomechanical arrays in more detail and discuss their relevance as a setup for the experimental implementation of coupled limit-cycle oscillators.

II. EFFECTIVE PHASE MODEL

In the system that we study, all oscillators are undergoing motion on a limit cycle, see Fig. 1. We start with the following equations ("Hopf equations"), which describe the effective phase and amplitude dynamics of these resonators close to the limit cycle [8,14]:

$$\dot{\varphi}_i = -\bar{\Omega} - (A_i - \bar{A})\frac{\partial \Omega}{\partial A}(\bar{A}) + \frac{F_i(t)}{m\Omega(A_i)A_i}\cos(\varphi_i),$$

$$\dot{A}_i = -\gamma(A_i - \bar{A}) + \frac{F_i(t)}{m\Omega(A_i)}\sin(\varphi_i). \tag{1}$$
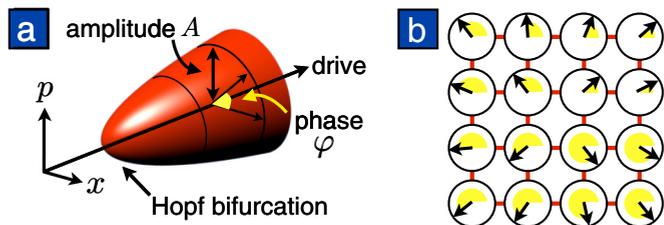

FIG. 1. (Color online) (a) A single Hopf oscillator undergoes dynamics on a limit cycle, with an amplitude set by external parameters (such as the drive providing the power) and a time-evolving phase $\varphi(t)$. (b) Array of coupled Hopf oscillators. Often, the system can be well described with a single degree of freedom per lattice site, the phase φ_i. Due to the coupling, the phases can lock and phase patterns can form.

Here $\bar{\Omega} = \Omega(\bar{A})$ is the frequency at the steady-state amplitude $\bar{A}$. The frequency-pull due to amplitude changes has been kept to leading order in the first line (in contrast to [8]) because it is known that this effect can play an important role in the synchronization of coupled oscillators [6,7]. γ is the rate at which the amplitude is forced back to the limit cycle, and $F_i(t)$ is the total force exerted on resonator i. For the physically most relevant spring-like coupling between nearest neighbors, which will be studied here, the force is given as $F_i = k \sum_{\langle j,i \rangle} A_j \cos(\varphi_j)$. The coupling constant is k, and $\langle j,i \rangle$ indicates nearest neighbor sites. We will see that for this coupling both the terms already discussed in [8] and the additional frequency-pulling term are important for the pattern formation and synchronization properties.

We consider the case of weak coupling $k/(m\bar{\Omega}^2) \ll 1$ and assume $\gamma/\bar{\Omega} \ll 1$, $(\bar{A}/\bar{\Omega})\partial\Omega/\partial A \ll 1$. Then the amplitude fluctuations around the steady state value are small and the amplitude dynamics can be integrated out (for details on this step, also about disorder, see [8,14] and Appendix A). We arrive at effective equations for the resonator phases. Keeping only the slow phase dynamics (and assuming identical resonators), we get

$$\dot{\varphi}_i = C \sum_{\langle j,i \rangle} \cos(\varphi_j - \varphi_i) + S_1 \sum_{\langle j,i \rangle} \sin(\varphi_j - \varphi_i)$$

$$+ S_2 \left\{ \sum_{\langle j,i \rangle} \sum_{\langle k,j \rangle} [\sin(2\varphi_j - \varphi_k - \varphi_i) - \sin(\varphi_k - \varphi_i)] \right.$$

$$\left. + \sum_{\langle j,i \rangle} \sum_{\langle k,i \rangle} \sin(\varphi_k + \varphi_j - 2\varphi_i) \right\} \quad (2)$$

with $C = k/2m\bar{\Omega}$, $S_1 = (C\bar{A}/\gamma)(\partial\Omega/\partial A)|_{A=\bar{A}}$, $S_2 = C^2/2\gamma$. We will call Eq. (2) the *Hopf-Kuramoto model*. It has been derived before in the context of optomechanics [8,14], but it holds generally for a set of weakly coupled Hopf oscillators. Our aim is to explore the dynamics of this model on a square lattice.

The term $\sin(\varphi_j - \varphi_i)$ of Eq. (2) is well known from the Kuramoto model [18], or, equivalently, the XY model [38]. Here the term arises from the amplitude-dependence of the frequency [6]. Both contributions in the first line of Eq. (2) have been derived previously for coupled limit-cycle oscillators, see [20]. They are linear in the coupling k. In contrast, the prefactor S_2 is of second order in k. However, as discussed in Sec. IV, in realistic scenarios γ and $\partial\Omega/\partial A$ can become small, such that the regime $S_2 \sim S_1, C$ is easily reached. The S_2 term can then have a profound influence on the pattern formation dynamics. The additional contribution also displays next-to-nearest-neighbor coupling of the phases, in spite of the underlying intrinsic nearest-neighbor coupling in the lattice assumed here. With the exception of [8,14] (where pattern formation was not considered), the S_2 term has not been discussed previously in the literature on models for the effective phase dynamics of coupled limit cycle oscillators, to the best of our knowledge.

We will first set the stage by highlighting several limiting cases of our model, some of which are known already. For $C = 0$, Eq. (2) can be rewritten in the form $\dot{\varphi}_i = -\partial U/\partial \varphi_i$. Hence, the system will slide down to a minimum of the potential U. In contrast, for non-vanishing C, such a potential does not exist and the system may never reach a stationary state (where $\dot{\varphi}_i$ is constant). The limiting case of Eq. (2) with $S_2 = 0$ has been studied before [39–43]. This is the Sakaguchi-Kuramoto model, usually written in the form $\dot{\varphi}_i = K \sum_{\langle j,i \rangle} \sin(\varphi_j - \varphi_i + \alpha)$ with $\tan(\alpha) = C/S_1$ and $K^2 = S_1^2 + C^2$.

The continuum limit of Eq. (2), which is valid for smooth phase fields, is given by

$$\dot{\varphi} = \mathcal{S}_1 \Delta\varphi - 2\mathcal{S}_2 \Delta^2\varphi - \mathcal{C}(\nabla\varphi)^2 + 4C, \quad (3)$$

where $\mathcal{S}_1 = S_1 a^2$, $\mathcal{S}_2 = S_2 a^4$, $\mathcal{C} = C a^2$, with lattice constant a, and Δ is the Laplace operator. In this model (with $\mathcal{S}_2 = 0$) it has been found that spirals can develop around singularities in the phase field [41,44]. Besides, it has been analyzed in connection with chemical turbulence in one dimension [45–47].

III. PATTERN FORMATION

The aim of this paper is to explore pattern formation in the full model, Eq. (2), in large two-dimensional arrays. Our main result is the pattern phase diagram discussed further below. The patterns we find will determine the phase synchronization dynamics of limit-cycle oscillators.
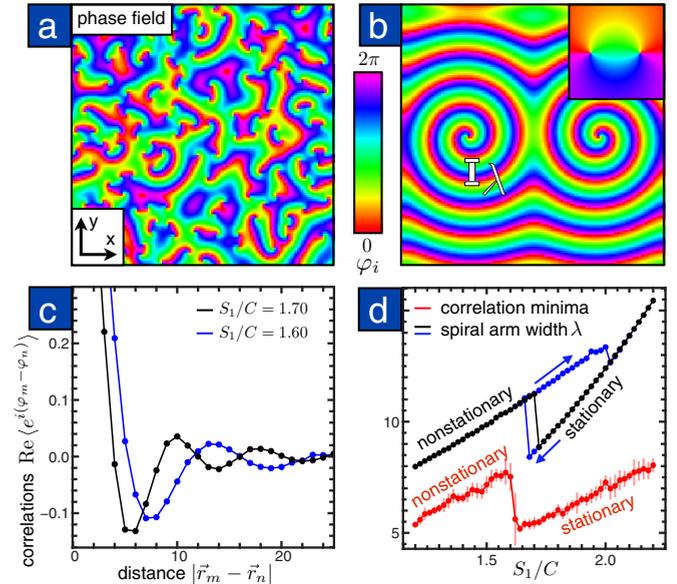

FIG. 2. (Color online) Spiral patterns and length scales in the Hopf-Kuramoto model. (a) Stationary spiral pattern emerging from random initial conditions for $S_1/C = 2.0$, $S_2/C = 0$ on a $N \times N$ square lattice ($N = 128$) with periodic boundary conditions. (b) Vortex–anti-vortex pair (see inset) winding up to a stationary spiral–anti-spiral pair with a characteristic spiral arm width λ. Parameters are like in (a). (c) Spatial correlations $\text{Re}\langle\exp[i(\varphi_m - \varphi_n)]\rangle$ as a function of the distance $|\vec{r}_m - \vec{r}_n|$ (rounded to the nearest integer). To obtain the data for (d), we extract the first correlation minimum position from parabolic fits and average over ten runs with different random initial conditions. (d) The location of the first correlation minimum [red (light grey)] and the spiral arm width λ from (b) (black), as a function of the ratio S_1/C, in units of the lattice constant. There can be hysteresis [blue (dark grey)].
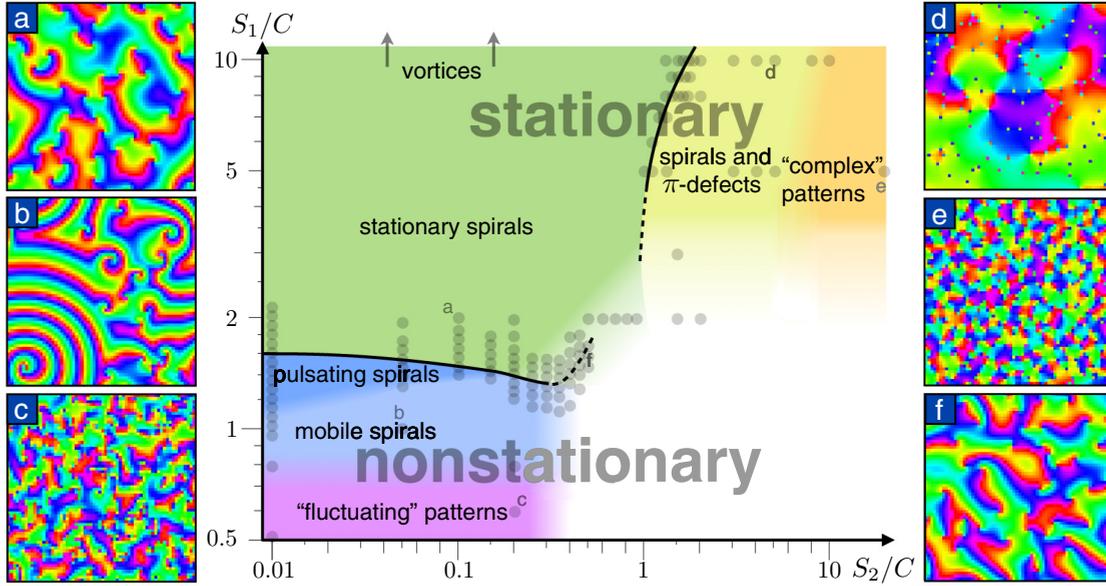
FIG. 3. (Color online) Pattern phase diagram of the Hopf-Kuramoto model, Eq. (2). Different colors indicate different patterns, which are discussed in the main text. Sharp transitions occur between stationary spirals and pulsating/mobile spirals (for small S_2/C), and in the appearance of "π defects". Point markers indicate parameters explored by numerical simulation. Some typical phase patterns are shown in the insets (a) to (f).

Our numerical results are mostly obtained from simulations with a random initial phase field, since that is the natural starting point in real systems (e.g., after switching on the pump laser or the feedback driving the oscillators into the limit cycle). After some transient dynamics, we often find patterns that do not change qualitatively any more on longer time scales. Moreover, in certain parameter regimes, we find nontrivial stationary patterns.

A typical final pattern of a simulation with large S_1/C is shown in Fig. 2(a). This pattern is stationary. It consists of many vortex-like "singularities", where the phase changes by 2π when going around in a closed loop. These points are surrounded by spiral structures. Spiral patterns in general are well known as a recurring motif in pattern formation [21,22,48]. Since they form an important part of the patterns we observe, we now briefly discuss the properties of isolated spirals, produced from an initial condition with a vortex in the phase field (Fig. 2(b)).

It is known that in related models, there is a transition from stationary spirals to nonstationary spirals, i.e., a situation when the spiral centers are no longer phase-locked to the bulk of the lattice [40,49]. We have discovered that this transition also gives rise to a jump in the width of the spiral arms, λ (Fig. 2). Outside of the jump, λ increases with increasing S_2/C and S_1/C (black curve in Fig. 2(d)). When sweeping the parameter ratio S_1/C up and down, we find hysteresis in the spiral arm width (blue line in Fig. 2(d)). The precise value at which the jump occurs can then depend on the parameter sweep rate. Our analysis illustrates that the microscopic details of the spiral center, on the scale of a few lattice sites, influence both the spiral arm width and the macroscopic pattern considerably. Because the structure of the spiral core is complicated, we cannot provide an analytical prediction for λ.

We now turn to the statistical properties of the patterns which evolve out of random initial conditions (see Fig. 2(a)), as they are directly relevant for experiments. The spatial correlations of the phase field are characterized by the correlator $\langle e^{i(\varphi_m - \varphi_n)} \rangle$, whose distance dependence is displayed in Fig. 2(c). We find an oscillatory structure connected to the presence of spiral arms. On top of that, there is an exponential decay, due to the presence of many randomly located spiral centers. The position of the first minimum in the oscillations indicates the distance approximately set by half a spiral arm width. The dependence of this position on the parameter S_1/C is shown as the red line in Fig. 2(d). Again, we find a sudden jump associated with the transition from stationary to nonstationary spiral centers. We note that the spiral arm width λ determined for isolated spirals does not agree completely with the length scale extracted from the oscillations of the correlator. The difference can be traced back to changes in the spiral core produced by the presence of other nearby spirals.

There are only two dimensionless parameters, S_1/C and S_2/C, that determine the properties of the final pattern. Therefore, a complete overview of the various regimes in our model is provided by the "pattern phase diagram" in Fig. 3. This summarizes the main results of our studies, and we now explain its features.

The transition discussed above, between stationary and nonstationary spirals, is sharp and can be traced up to intermediate values of S_2/C. In addition, we find two classes of nonstationary spirals: "pulsating" spirals, where the core keeps orbiting in a small circle around a fixed location [49], and truly mobile spirals that move through the whole lattice. We will comment on their dynamics later. We have not observed a sharp transition between the two regimes (Fig. 3). At larger S_2/C, the transition is directly from stationary to mobile spirals.

When decreasing the parameter S_1/C even further, we find a crossover to "fluctuating" patterns, see Fig. 3(c). These are nonstationary patterns with a complicated phase structure on the scale of the lattice. For the special case $S_2 = 0$, the location of the crossover (around $S_1/C \sim 0.8$) matches the result obtained in [42].

The crucial macroscopic length scale of the Hopf-Kuramoto model, i.e., the spiral arm width, grows with increasing S_2/C. In view of that, it is surprising to see microscopic structures appearing at larger values of this parameter. Indeed, we find a sharp transition from the domain of "stationary spirals" to stationary patterns that contain "π defects", see Fig. 3(d). These are point defects which are offset by a phase difference of roughly π from the smooth surrounding phase field. The stability of a single π defect on a homogeneous background can be analyzed by semi-analytical linear stability analysis (in the limit $C \to 0$; for details, see Appendix B), which gives the critical value $S_2/S_1 = 0.107$. This defines the asymptote for the transition line in Fig. 3. Above the critical value, the π-defect patterns form a fixed point of the dynamics and can be reached from random initial conditions. In contrast to the pure spiral patterns, these patterns resolve the structure of the lattice and hence form a fundamentally different phase. Obviously, they cannot appear in the continuum model, Eq. (3).

When increasing the parameter value S_2/C further, the density of π defects increases until we observe a smooth transition to "complex" patterns. These are stationary patterns with a complicated phase structure on the scale of the lattice, see Fig. 3(e).

In the future, order parameters for the transitions shown in Fig. 3 could be studied, although this will require larger lattices and a large number of runs for sufficient statistical precision. For example, the transition from a vanishing to a finite variance of the phase velocity field characterizes the transition from stationary to nonstationary patterns, and we have observed this in preliminary numerical investigations (not shown here). Similarly, a finite number of π defects signals the transition from the stationary spiral regime to the "spirals and π defects" region.

For a large region in parameter space, trivial phase-homogeneous states would also be stable. However, when starting from random initial conditions in large arrays (which is what we do here), typically a lot of spiral–anti-spiral pairs nucleate initially. Not all of these pairs annihilate. This is why we never observe a phase-homogeneous state in our numerical simulations. That behavior could change in principle if a small amount of noise were added, because that would increase the spiral mobility.

Finally, we note that the white region in the phase diagram could not be accessed due to the significant increase of timescales. Apart from that, we have discussed all phases in the Hopf-Kuramoto model, for positive parameters. Changing the sign of C or S_1 will not give qualitatively different results: The emerging patterns can be reconstructed from the patterns discussed above by the transformations $\varphi_{m,n} \to -\varphi_{m,n}$ for a sign change of C, and $\varphi_{m,n} \to -\varphi_{m,n} + (-1)^{m+n}\pi/2$ for a sign change of S_1. This works because of the symmetries of the sine and cosine functions in Eq. (2) under a sign change or a shift by π of their arguments. For example, for a negative sign of S_1, we obtain checkerboard-type patterns that involve the smallest wavelength allowed by the lattice. Note that in the
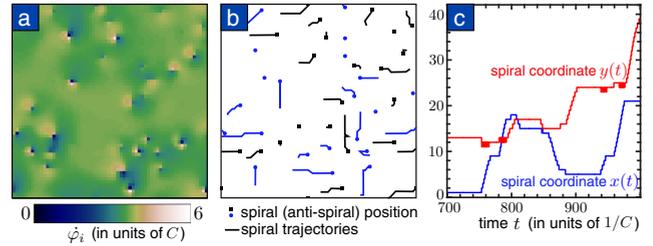

FIG. 4. (Color online) Spiral motion in the Hopf-Kuramoto model. (a) Instantaneous phase velocity field $\dot{\varphi}_i$ after a (long) integration time $T = 1000/C$. Mobile spiral centers are visible as local inhomogeneities in $\dot{\varphi}_i$. Some stationary spirals (not visible) exist in the uniform regions. Parameters are $S_1/C = 1.6$, $S_2/C = 0.5$, $N = 64$. The corresponding phase field is shown in Fig. 3(f). (b) Spiral positions at time T. The lines are the spiral trajectories (from $T - 15/C$ to T; the trajectories have been slightly smoothened for clarity). (c) Spiral dynamics of a single spiral over a longer period of time. It can be seen that the spiral remains fixed for some time before starting to move again (this is usually induced via a kick by a nearby mobile spiral). The spiral preferably moves in the cartesian directions set by the lattice.

continuum model, Eq. (3), this regime will likely give rise to phase turbulence. The transformations discussed above work for all values of S_2. However, changing the sign of S_2 will lead to different patterns. These involve structure on the scale of the lattice, where phase differences of roughly $\pi/2$ play an important role. We will not discuss these patterns, because for coupled Hopf oscillators S_2 is positive.

We now turn to a more detailed discussion of the spiral motion and interaction (see also [50] for the continuum case, at $S_2 = 0$. For a more general discussion of spiral motion and interaction in the related context of the complex Ginzburg-Landau equation, see the review [22]). We will focus on the influence of the parameter S_2/C, which has not been studied before. Whenever we observe mobile spirals, a fraction of the spirals and anti-spirals eventually annihilate. In some cases, they can also be created dynamically. We observe that the spirals move through the array almost independent of one another for small S_2/C, whereas they tend to move in pairs for larger values of this parameter. For large values of S_2/C, mobile and stationary spirals can even coexist, see Fig. 4. Depending on initial conditions, the final state can then be nonstationary or stationary (if all mobile spirals annihilate).

There is also a parameter regime where π defects, stationary and mobile spirals can all be present and interact: Upon the annihilation of a spiral–anti-spiral pair, a π defect can be left behind. This happens more often for larger values of S_2/C. When a mobile spiral approaches a π defect, it can induce the dissolution of the defect into a spiral–anti-spiral pair. However, the mobile spiral can also move across the defect and make it vanish. All these interactions play an important role even at late times.

IV. EXPERIMENTAL IMPLEMENTATION

Experimental studies of the patterns discussed in this work could be implemented by direct local electrical readout of the motion in electrically coupled nanomechanical resonator

arrays [3], or by optical readout of the motion in future optomechanical arrays based on optomechanical crystals [35–37] or other platforms. Optomechanical arrays have attracted a lot of attention recently, e.g., with respect to collective interactions [9,26,27], reservoir engineering [30], many-body dynamics [8,14], photon propagation [31], topological phase transitions [32,33], and Dirac physics [34]. These devices consist of an array of localized mechanical modes, each of them coupled to one optical mode, driven by a laser. The major advantage of these systems is their optical tunability, which allows to engineer the transport of photons and phonons at will, as well as to read out the dynamics via the light field. More recently, a very promising tow-dimensional (2D) structure (a so-called 'snowflake' photonic crystal [36]) has been realized, which shows simultaneously an optical and acoustic bandgap. This will naturally form the basis of 2D arrays, with an array of defect modes coupled by nearest-neighbor tunneling of photons and phonons. 2D optomechanical arrays are a very promising platform for synchronizing (opto-)mechanical oscillators, thereby improving their stability against noise. Pattern formation in this context is crucial in affecting the synchronization dynamics.

By varying the driving laser power and detuning in optomechanical arrays, the parameters of the Hopf-Kuramoto model could be tuned. Simulations of single optomechanical cells, where we extracted the phenomenological parameters γ, $\bar{A}$ and $(\partial\Omega/\partial A)|_{A=\bar{A}}$, suggest that all the important regions of the pattern phase diagram could be explored. Near the Hopf bifurcation, $\gamma \lesssim C$ can be reached (since $\gamma \to 0$), so $S_2 \gtrsim C$. Furthermore, $S_2 \gtrsim S_1$ holds as well for sufficient coupling k, when $\bar{A}(\partial\Omega/\partial A)|_{A=\bar{A}} \lesssim C$. The motion can be read out by observing the light scattered from the sample. The intensity of the light scattered with wave vector transfer $\vec{q}$ is related to the structure factor (see Appendix C), i.e., the spatial Fourier transform (at $\vec{q}$) of the phase correlator $\langle e^{i(\varphi_l - \varphi_j)}\rangle_t$. As was discussed above, this correlator contains information about the phase pattern, for example about the spiral properties, see Fig. 2.

In a typical experiment, the frequencies will be disordered, but first simulations with small disorder (where the natural frequencies in the Hopf-Kuramoto model have been drawn from a Gaussian distribution with a standard deviation of $0.1C$) do not show qualitative changes of the patterns we discussed. However, initially mobile spirals could be pinned at sites with lower frequencies [40]. In simulations with strong disorder, concentric waves ("target patterns", as discussed in [51]) can show up. We did not study the influence of disorder in the more fundamental Hopf equations (1). In addition to the disorder in frequencies (briefly discussed here), this would also lead to disorder in the parameters C, S_1, and S_2.

V. CONCLUSION

The variety of patterns summarized in Fig. 3 are important for synchronization dynamics and applications. For example, finite phase-differences across the array (in stationary patterns) will reduce the total power output of the collective oscillator, and the mere presence of spirals can reduce the robustness against noise [10]. Finite frequency-differences (in nonstationary patterns) reduce the frequency stability. Tuning the parameters into suitable regions will optimize the array's

properties. Future theoretical studies of the Hopf-Kuramoto model could include noise, which may lead to interesting effects, as discussed for similar models in [19]. In that context, as well as in the deterministic case, the role of spiral motion and interaction could be analyzed in more detail.

APPENDIX A: DERIVATION OF THE HOPF-KURAMOTO MODEL

In this Appendix, we derive the Hopf-Kuramoto model, Eq. (2) in the main text, from the following general Hopf equations:

$$\dot{\varphi}_i = -\bar{\Omega}_i - \frac{\partial\Omega_i}{\partial A_i}\Big|_{A_i=\bar{A}}(A_i - \bar{A}_i) + \frac{F_i(t)}{m_i\Omega_i(A_i)A_i}\cos\varphi_i,$$
$$\text{(A1)}$$

$$\dot{A}_i = -\gamma(A_i - \bar{A}_i) + \frac{F_i(t)}{m_i\Omega_i(A_i)}\sin\varphi_i. \quad \text{(A2)}$$

Here, $\Omega_i(A_i)$ is the amplitude-dependent frequency of the oscillator at site i, m_i is its mass, $\bar{A}_i$ is its steady-state amplitude, and $\bar{\Omega}_i = \Omega_i(\bar{A}_i)$ is the frequency at the steady-state amplitude. Other symbols have the same meaning as in the main text. The second term on the right-hand side of Eq. (A1) arises from the expansion of $\Omega_i(A_i)$ around the steady-state amplitude $\bar{A}_i$. For reasons that will become clear later, $\Omega_i(A_i)$ has not been expanded in the force terms in Eqs. (A1) and (A2). We assume that the oscillators are coupled by spring-like nearest-neighbor couplings so that the forces $F_i(t)$ are given by

$$F_i = \sum_{\langle j,i\rangle} k_{ij}x_j = \sum_{\langle j,i\rangle} k_{ij}A_j\cos\varphi_j, \quad \text{(A3)}$$

where $\langle j,i\rangle$ denotes the nearest neighbors j of site i and $k_{ij} = k_{ji}$ are spring constants.

The derivation of the Hopf-Kuramoto model involves the adiabatic elimination of the amplitude fluctuations $\delta A_i = A_i - \bar{A}_i$, as well as leading-order expansions in the dimensionless, small parameters $k_{ij}/(m_i\bar{\Omega}_i^2)$, $(\bar{A}_i/\Omega_i)\partial\Omega_i/\partial A_i$, and $\gamma/\bar{\Omega}_i$. These parameters and the relative amplitude fluctuations $\delta A_i/\bar{A}$ are assumed to be of the same order of smallness. Below, we will also only keep slowly varying terms. The derivation can also be found in [8]. For some more details, see the Supplemental Material of [14].

In order to eliminate the amplitude fluctuations, we rewrite Eq. (A2) in terms of the amplitude fluctuations and formally integrate the equation

$$\delta\dot{A}_i = -\gamma\,\delta A_i + \frac{\sin\varphi_i}{m_i\Omega_i(A_i)}\sum_{\langle j,i\rangle} k_{ij}(\bar{A}_i + \delta A_i)\cos\varphi_j \quad \text{(A4)}$$

to obtain the long-time limit result

$$\delta A_i(t) = \frac{1}{m_i\Omega_i(A_i)}\int_{-\infty}^{t} dt'\, e^{-\gamma(t-t')}\sin\varphi_i(t')$$
$$\times \sum_{\langle j,i\rangle} k_{ij}[\bar{A}_i + \delta A_i(t')]\cos\varphi_j(t'). \quad \text{(A5)}$$

Since the integrand is proportional to k_{ij}, to leading order it suffices to evaluate $\varphi_i(t')$ to zeroth order in the expansion parameters, i.e., $\varphi_i(t') \simeq \varphi_i(t) - \Omega_i(t - t')$. Thus, we find

$$\delta A_i \simeq \sum_{\langle j,i \rangle} \frac{\bar{A}_i k_{ij}}{m_i \Omega_i(A_i)} \int_{-\infty}^{t} dt' \, e^{-\gamma(t-t')} \sin[\varphi_i(t) - \Omega_i(t - t')]$$

$$\times \cos[\varphi_j(t) - \Omega_j(t - t')]. \quad \text{(A6)}$$

The integral can easily be evaluated. To leading order in $\gamma/\bar{\Omega}_i$, the result reduces to

$$\delta A_i \simeq \sum_{\langle j,i \rangle} \frac{\bar{A}_i k_{ij}}{m_i \Omega_i(A_i)} \frac{\sin(\varphi_i - \varphi_j)}{2\gamma}. \quad \text{(A7)}$$

To first order in the amplitude fluctuations, the equations of motion for the oscillator phases (A1) can be expanded as

$$\dot{\varphi}_i \simeq -\bar{\Omega}_i - \left. \frac{\partial \Omega_i}{\partial A_i} \right|_{A_i = \bar{A}_i} \delta A_i$$

$$+ \frac{\cos \varphi_i}{m_i \Omega_i(A_i)} \sum_{\langle j,i \rangle} k_{ij} \left(1 + \frac{\delta A_j - \delta A_i}{\bar{A}} \right) \cos \varphi_j. \quad \text{(A8)}$$

Corrections to $\Omega_i(A_i) \simeq \Omega_i(\bar{A}_i) = \bar{\Omega}_i$ are proportional to both $(\bar{A}_i/\Omega_i)\partial\Omega_i/\partial A_i$ and $\delta A_i/\bar{A}_i$ so that they are of second order. In the second term on the right-hand side, these are significant, but, since in the third term they are multiplied by another k_{ij}, they can be neglected there. Inserting Eq. (A7), again replacing $\Omega_i(A_i)$ in the denominator by $\bar{\Omega}_i$, we finally obtain

$$\dot{\varphi}_i \simeq -\bar{\Omega}_i + \left. \frac{\partial \Omega_i}{\partial A_i} \right|_{A_i = \bar{A}_i} \sum_{\langle j,i \rangle} \frac{\bar{A}_i k_{ij}}{m_i \bar{\Omega}_i} \frac{\sin(\varphi_j - \varphi_i)}{2\gamma}$$

$$+ \sum_{\langle j,i \rangle} \frac{k_{ij} \cos(\varphi_j - \varphi_i)}{2 m_i \bar{\Omega}_i}$$

$$+ \sum_{\langle j,i \rangle} \sum_{\langle k,j \rangle} \frac{k_{ij}^2}{8\gamma m_i^2 \bar{\Omega}_i^2} (\sin(2\varphi_j - \varphi_i - \varphi_k) - \sin(\varphi_k - \varphi_i))$$

$$+ \sum_{\langle j,i \rangle} \sum_{\langle k,i \rangle} \frac{k_{ij}^2}{8\gamma m_i^2 \bar{\Omega}_i^2} \left(\sin(\varphi_k + \varphi_j - 2\varphi_i) \right), \quad \text{(A9)}$$

where we have also only kept slowly varying contributions by applying the approximations $\cos \varphi_i \cos \varphi_j \simeq \frac{1}{2} \cos(\varphi_i - \varphi_j)$, $\cos \varphi_i \cos \varphi_j \sin(\varphi_j - \varphi_k) \simeq \frac{1}{4}\{\sin(\varphi_i - \varphi_k) - \sin(\varphi_i + \varphi_k - 2\varphi_j)\}$, and $\cos \varphi_i \cos \varphi_j \sin(\varphi_i - \varphi_k) \simeq \frac{1}{4}\{\sin(2\varphi_i - \varphi_j - 2\varphi_k) - \sin(\varphi_k - \varphi_j)\}$. In the special case of identical oscillators $\bar{\Omega}_i = \bar{\Omega}$, $m_i = m$ and $\bar{A}_i = \bar{A}$ for all i and uniform couplings $k_{ij} = k$ for all neighbors i, j, this obviously reduces to Eq. (2) in the main text, where we have also neglected the trivial term $-\bar{\Omega}$ on the right-hand side.

APPENDIX B: SEMI-ANALYTICAL STABILITY ANALYSIS OF POINT DEFECTS

In this Appendix, we present the analysis of the stability of a single π defect on a homogeneous background phase field for the Hopf-Kuramoto model [Eq. (2) in the main text] with $C = 0$. For this case, the aforementioned phase configuration, which we call φ^0, is a fixed point of the dynamics, i.e., $\dot{\varphi}_i^0 = 0$
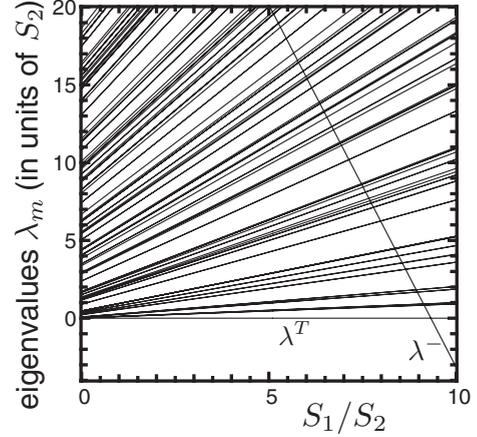

FIG. 5. The eigenvalues λ_m of the Hessian $\partial^2 U/(\partial\varphi_i \partial\varphi_j)$ for a homogeneous phase configuration with a single π defect, as a function of the parameter S_1/S_2 for a lattice of size 20×20. Note the eigenvalue λ^- leading to the instability of the π defect. The zero eigenvalue λ^T belongs to the translational mode of the phase configuration.

for all sites i. Besides, the equation of motion can be written as $\dot{\varphi}_i = -\frac{\partial}{\partial\varphi_i} U$ with the potential

$$U(\varphi_1, \ldots, \varphi_{N^2}) = \sum_i \left\{ \sum_{\langle j,i \rangle} \frac{S_1}{2} [1 - \cos(\varphi_j - \varphi_i)] \right.$$

$$\left. + S_2 \left[\sum_{\langle j,i \rangle} \sin(\varphi_j - \varphi_i) \right]^2 \right\}. \quad \text{(B1)}$$

We calculate the Hessian $\partial^2 U/(\partial\varphi_i \partial\varphi_j)$ and evaluate its eigenvalues for the phase configuration φ^0 numerically. If at least one of the eigenvalues is negative, the configuration is unstable. A single eigenvalue, corresponding to the translational mode of the system, might vanish without disturbing our analysis. We always find this zero eigenvalue. For small values of S_1/S_2, all the other eigenvalues are positive, which means that π defects are stable (see Fig. 5). With increasing S_1/S_2, the eigenvalues change linearly with this parameter. A single eigenvalue $\lambda^-(S_1/S_2)$ has a negative slope, so it becomes negative at some critical value $(S_1/S_2)^c \approx 9.34$, rendering the phase configuration unstable. This gives the (inverse) value $S_2/S_1 \approx 0.107$ given in the main text.

APPENDIX C: READ-OUT OF THE MECHANICAL RESONATOR PHASE FIELD

Here, we will show how the intensity of the light reflected from an optomechanical array is related to the spatial Fourier transform of the phase correlator. The intensity of the light reflected from an optomechanical array with lattice sites at $\vec{r}_j$ is given as

$$|E(\vec{q})|^2 / |E^{\text{in}}|^2 = \left| \sum_j e^{-i\vec{q}\cdot\vec{r}_j} e^{i\theta_j} \right|^2. \quad \text{(C1)}$$

The phase of the light reflected from site j is $\theta_j = \theta^{\max}\cos(\varphi_j)$, where $\theta^{\max}$ depends on the system parameters. If the mechanical frequency is much smaller than the cavity intensity decay rate κ, then $\theta^{\max} = AG/\kappa$, with the mechanical amplitude A and the optical frequency shift per displacement G [52]. For small $\theta^{\max}$, Eq. (C1) can be expanded and we get

$$|E(\vec{q})|^2/|E^{\mathrm{in}}|^2$$

$$\approx \sum_{j,l} e^{-i\vec{q}\cdot(\vec{r}_l-\vec{r}_j)}\left[1+i(\theta_l-\theta_j)-\frac{1}{2}(\theta_l-\theta_j)^2\right]. \quad \text{(C2)}$$

We average over time, use $\langle\theta_j\rangle_t=0$ and $\langle\theta_j^2\rangle_t=(\theta^{\max})^2/2$, and arrive at

$$\langle|E(\vec{q})|^2/|E^{\mathrm{in}}|^2\rangle_t=\left[1-\frac{(\theta^{\max})^2}{2}\right]\left|\sum_j e^{i\vec{q}\cdot\vec{r}_j}\right|^2$$

$$+\left\langle\left|\sum_j e^{i\vec{q}\cdot\vec{r}_j}\theta_j\right|^2\right\rangle_t. \quad \text{(C3)}$$

For large arrays, the first term will only give contributions very close to $\vec{q}=0$. For small arrays, these contributions may have to be eliminated by calibrating the measurement device with a known phase field. The second term can be evaluated to give

$$\left\langle\left|\sum_j e^{i\vec{q}\cdot\vec{r}_j}\theta_j\right|^2\right\rangle_t$$

$$=\frac{(\theta^{\max})^2}{2}\sum_{j,l}e^{-i\vec{q}\cdot(\vec{r}_l-\vec{r}_j)}\mathrm{Re}\langle e^{i(\varphi_l-\varphi_j)}\rangle_t. \quad \text{(C4)}$$

On the right-hand side of this equation, the discrete Fourier transform of the correlations in the system appears. We have analyzed similar correlation functions in connection with the spiral length scale, see Fig. 2 in the main text. From Eq. (C4) we see that we can learn about the correlations by detecting the intensity of the reflected light. An example for the part of
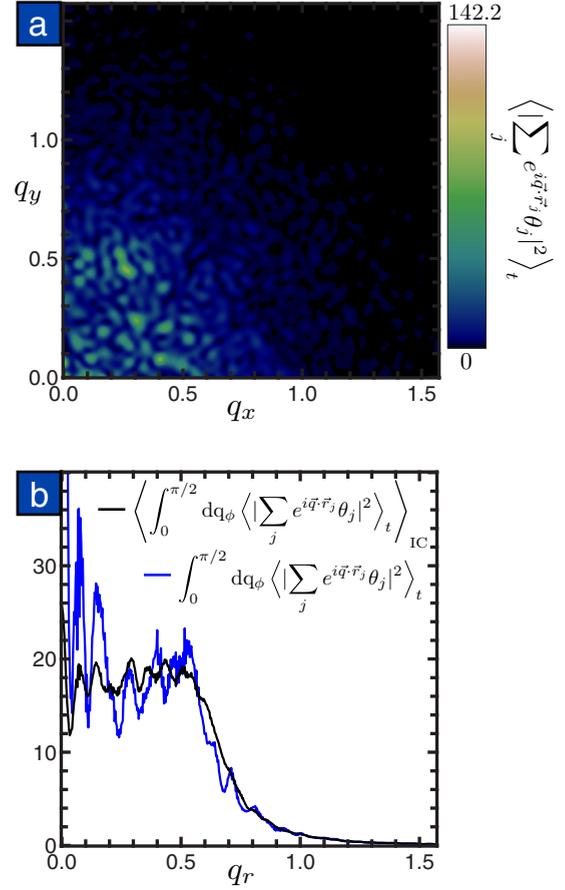

FIG. 6. (Color online) (a) Partial intensity $\langle|\sum_j e^{i\vec{q}\cdot\vec{r}_j}\theta_j|^2\rangle_t$ of the light reflected from the phase field given in Fig. 2(a). Parameter $\theta^{\max}=0.01$. (b) Partial intensity $\langle|\sum_j e^{i\vec{q}\cdot\vec{r}_j}\theta_j|^2\rangle_t$ in dependance on the radial coordinate $q_r=\sqrt{q_x^2+q_y^2}$, averaged over 11 different random initial phase configurations (black) and for a single phase configuration as in (a) (blue).

the detected light intensity that is given in Eq. (C4) is given in Fig. 6.

[1] J. Kurths, A. Pikovsky, and M. Rosenblum, *Synchronization: A Universal Concept in Nonlinear Sciences* (Cambridge University Press, Cambridge, England, 2001).

[2] M. Bagheri, M. Poot, L. Fan, F. Marquardt, and H. X. Tang, Phys. Rev. Lett. **111**, 213902 (2013).

[3] M. H. Matheny, M. Grau, L. G. Villanueva, R. B. Karabalin, M. C. Cross, and M. L. Roukes, Phys. Rev. Lett. **112**, 014101 (2014).

[4] M. Zhang, G. S. Wiederhecker, S. Manipatruni, A. Barnard, P. McEuen, and M. Lipson, Phys. Rev. Lett. **109**, 233906 (2012).

[5] M. Zhang, S. Shah, J. Cardenas, and M. Lipson, arXiv:1505.02009 (2015).

[6] M. C. Cross, A. Zumdieck, R. Lifshitz, and J. L. Rogers, Phys. Rev. Lett. **93**, 224101 (2004).

[7] M. C. Cross, J. L. Rogers, R. Lifshitz, and A. Zumdieck, Phys. Rev. E **73**, 036205 (2006).

[8] G. Heinrich, M. Ludwig, J. Qian, B. Kubala, and F. Marquardt, Phys. Rev. Lett. **107**, 043603 (2011).

[9] C. A. Holmes, C. P. Meaney, and G. J. Milburn, Phys. Rev. E **85**, 066203 (2012).

[10] John-Mark A. Allen and M. C. Cross, Phys. Rev. E **87**, 052902 (2013).

[11] M. C. Cross, Phys. Rev. E **85**, 046214 (2012).

[12] T. E. Lee and M. C. Cross, Phys. Rev. Lett. **106**, 143001 (2011).

[13] G. L. Giorgi, F. Galve, G. Manzano, P. Colet, and R. Zambrini, Phys. Rev. A **85**, 052101 (2012).

[14] M. Ludwig and F. Marquardt, Phys. Rev. Lett. **111**, 073603 (2013).

[15] A. Mari, A. Farace, N. Didier, V. Giovannetti, and R. Fazio, Phys. Rev. Lett. **111**, 103605 (2013).

[16] S. Walter, A. Nunnenkamp, and C. Bruder, Annalen der Physik **527**, 131 (2015).

[17] T. E. Lee and H. R. Sadeghpour, Phys. Rev. Lett. **111**, 234101 (2013).

[18] Y. Kuramoto, in *International Symposium on Mathematical Problems in Theoretical Physics*, Lecture Notes in Physics, Vol. 39, edited by H. Araki (Springer, Berlin-Heidelberg, 1975), pp. 420–422.

[19] J. Acebrón, L. Bonilla, C. Pérez Vicente, F. Ritort, and R. Spigler, Rev. Mod. Phys. **77**, 137 (2005).

[20] R. Lifshitz, E. Kenig, and M. C. Cross, in *Fluctuating Nonlinear Oscillators*, edited by M. I. Dykman (Oxford University Press, Oxford, 2012), Chap. 11.

[21] M. C. Cross and P. C. Hohenberg, Rev. Mod. Phys. **65**, 851 (1993).

[22] I. S. Aranson and L. Kramer, Rev. Mod. Phys. **74**, 99 (2002).

[23] D. E. Chang, A. H. Safavi-Naeini, M. Hafezi, and O. Painter, New J. Phys. **13**, 023003 (2011).

[24] M. Schmidt, M. Ludwig, and F. Marquardt, New J. Phys. **14**, 125005 (2012).

[25] U. Akram, W. Munro, K. Nemoto, and G. J. Milburn, Phys. Rev. A **86**, 042306 (2012).

[26] A. Xuereb, C. Genes, and A. Dantan, Phys. Rev. Lett. **109**, 223601 (2012).

[27] M. Bhattacharya and P. Meystre, Phys. Rev. A **78**, 041801 (2008).

[28] A. Xuereb, A. Imparato, and A. Dantan, New J. Phys. **17**, 055013 (2015).

[29] A. Xuereb, C. Genes, G. Pupillo, M. Paternostro, and A. Dantan, Phys. Rev. Lett. **112**, 133604 (2014).

[30] A. Tomadin, S. Diehl, M. D. Lukin, P. Rabl, and P. Zoller, Phys. Rev. A **86**, 033821 (2012).

[31] W. Chen and A. A. Clerk, Phys. Rev. A **89**, 033854 (2014).

[32] V. Peano, C. Brendel, M. Schmidt, and F. Marquardt, arXiv:1409.5375 (2014).

[33] M. Schmidt, S. Keßler, V. Peano, O. Painter, and F. Marquardt, arXiv:1502.07646 (2015).

[34] M. Schmidt, V. Peano, and F. Marquardt, New J. Phys. **17**, 023025 (2015).

[35] M. Eichenfield, J. Chan, R. M. Camacho, K. J. Vahala, and O. Painter, Nature **462**, 78 (2009).

[36] A. H. Safavi-Naeini, J. T. Hill, S. Meenehan, J. Chan, S. Gröblacher, and O. Painter, Phys. Rev. Lett. **112**, 153603 (2014).

[37] A. H. Safavi-Naeini and O. Painter, Opt. Express **18**, 14926 (2010).

[38] J. M. Kosterlitz and D. J. Thouless, J. Phys. C: Solid State Physics **6**, 1181 (1973).

[39] H. Sakaguchi and Y. Kuramoto, Prog. Theor. Phys. **76**, 576 (1986).

[40] H. Sakaguchi, S. Shinomoto, and Y. Kuramoto, Prog. Theor. Phys. **79**, 1069 (1988).

[41] Y. Kuramoto, Prog. Theor. Phys. Supplement **79**, 223 (1984).

[42] P.-J. Kim, T.-W. Ko, H. Jeong, and H.-T. Moon, Phys. Rev. E **70**, 065201 (2004).

[43] K. Wiesenfeld, P. Colet, and S. H. Strogatz, Phys. Rev. E **57**, 1563 (1998).

[44] Y. Kuramoto and T. Yamada, Prog. Theor. Phys. **56**, 724 (1976).

[45] T. Yamada and Y. Kuramoto, Prog. Theor. Phys. **56**, 681 (1976).

[46] Y. Kuramoto and T. Tsuzuki, Prog. Theor. Phys. **55**, 356 (1976).

[47] Y. Kuramoto, Prog. Theor. Phys. **63**, 1885 (1980).

[48] A. T. Winfree, Science **175**, 634 (1972).

[49] J. E. Paullet and G. B. Ermentrout, SIAM J. Appl. Math. **54**, 1720 (1994).

[50] I. S. Aranson, L. Kramer, and A. Weber, Phys. Rev. Lett. **67**, 404 (1991).

[51] B. Blasius and R. Tönjes, Phys. Rev. Lett. **95**, 084101 (2005).

[52] M. Aspelmeyer, T. J. Kippenberg, and F. Marquardt, Rev. Mod. Phys. **86**, 1391 (2014).